ACS NANO

www.acsnano.org

ARTICLE

Nondisassembly Repair of Degraded $LiFePO_4$ Cells via Lithium Restoration from the Solid Electrolyte Interphase

Xiaodi Zhao, Hao Chen, Hu Wu, Yumeng Zhao,* and Jiayan Luo*

Cite This: *ACS Nano* 2024, 18, 21125–21134

Read Online

ACCESS | Metrics & More | Article Recommendations | Supporting Information

ABSTRACT: **The disposal of degraded batteries will be a severe challenge with the expanding market demand for lithium iron phosphate ($LiFePO_4$ or LFP) batteries. However, due to a lack of economic and technical viability, conventional metal extraction and material regeneration are hindered from practical application. Herein, we propose a nondisassembly repair strategy for degraded cells through a lithium restoration method based on deep discharge, which can elevate the anodic potential to result in the selective oxidative decomposition and thinning of the solid electrolyte interphase (SEI) on the graphite anode. The decomposed SEI acts as a lithium source to compensate for the Li loss and eliminate Li−Fe antisite defects for degraded LFP. Through this design, the repaired pouch cells show improved kinetic characteristics, significant capacity restoration, and an extended lifespan. This proposed repair scheme relying on SEI rejuvenation is of great significance for extending the service life and promoting the secondary use of degraded cells.**

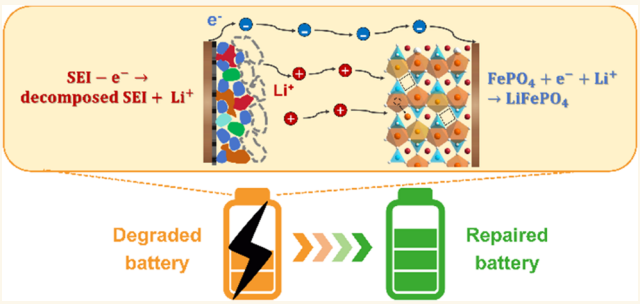

KEYWORDS: *degraded LFP cells, cell repair, Li restoration, SEI rejuvenation, deep discharge, nondisassembly*

The market share of olivine lithium iron phosphate ($LiFePO_4$ or LFP) batteries is growing rapidly due to their low cost, long cycle life, and high safety, especially in electric vehicles and grid energy storage.[1,2] Batteries degrade during long-term cycling and are considered end-of-life when the capacity drops to 80%.[3,4] Attributed to the low intrinsic value of LFP, conventional element-level metal extraction is not economically viable.[3] Direct regeneration is considered potentially profitable for its retention of embedded energy in the cathode structure.[5−7] However, technical constraints remain the most significant barrier to its practical application.[8,9] Using the high-purity degraded cathode active material as the raw material, direct regeneration has demonstrated close to 100% recovery on a lab scale, whereas the "cathode black mass" obtained from practical mechanical disassembly is actually a mixture containing various impurities, which is challenging to be removed entirely or controlled on a large scale.[8,10] As a result, the performance consistency of directly regenerated cathode materials cannot be guaranteed.[11−13] It is therefore imperative to develop scalable and cost-effective strategies to enable the residual value of degraded batteries to be utilized.

The capacity degradation of lithium-ion batteries (LIBs) is associated with lithium loss due to thickening of the solid electrolyte interphase (SEI) and undesired phase transformation.[5] Regarding the cathode materials, it is worth noting that LFP retains a very stable olivine structure after a long cycling period, and its performance degradation is mainly attributed to lithium deficiency.[14,15] Also, irreversible lithium extraction would induce Li/Fe cation site exchange, forming antisite defects that hinder Li^+ migration.[16,17] Luckily, these degradations can be effectively repaired by lithium replenishment and Fe(III) reduction, though without the use of thermal annealing,[18−20] which is indispensable for the regeneration of layered oxide ternary (NCM) batteries with severe structure damage.[21,22] The relatively simple repair principle of degraded LFP provides potential opportunities for directly regenerating degraded LFP electrodes in situ while maintaining their integrity.

Received: March 7, 2024
Revised: July 24, 2024
Accepted: July 26, 2024
Published: August 3, 2024

https://doi.org/10.1021/acsnano.4c03221
ACS Nano 2024, 18, 21125−21134

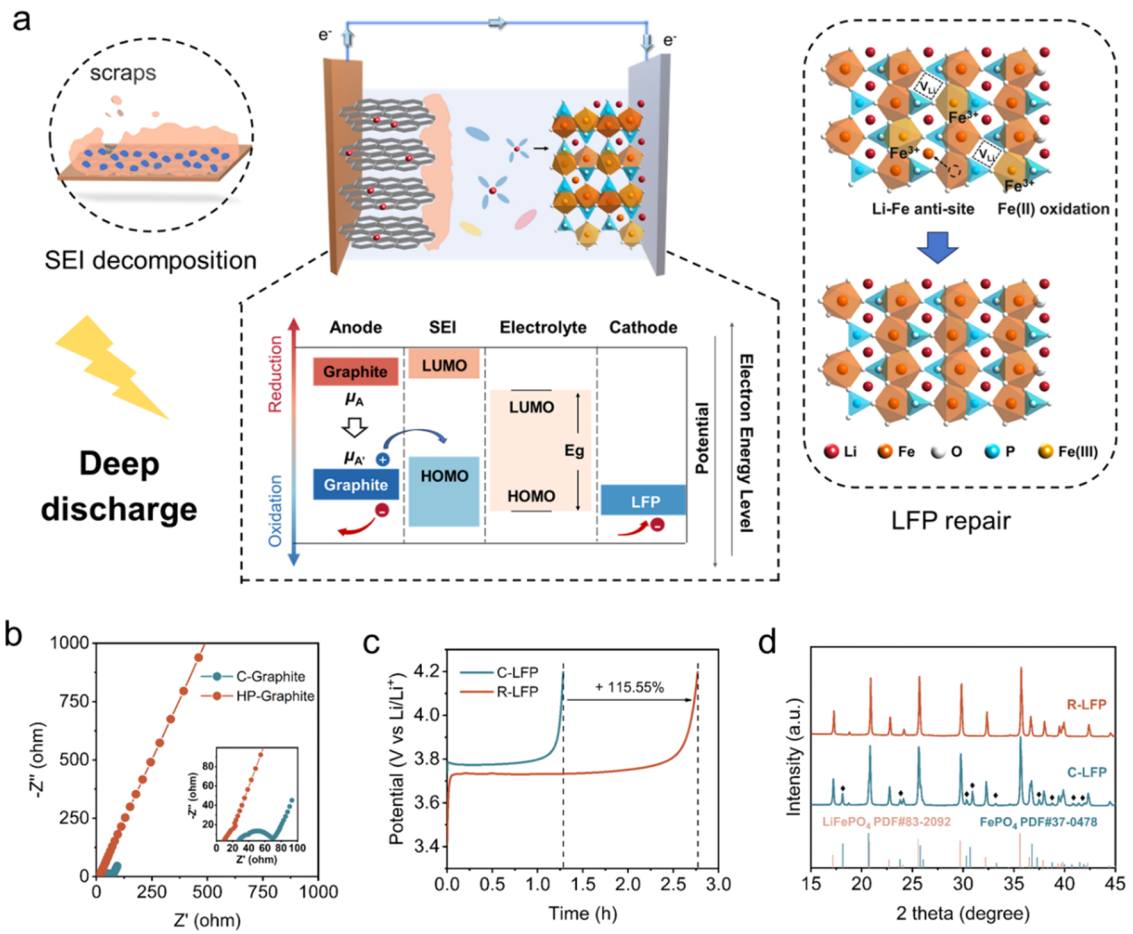

Figure 1. Design concept of the LFP cell repair strategy based on deep discharge. (a) Working mechanism of the repair strategy. (b) Electrochemical impedance spectroscopy (EIS) for C-Graphite and HP-Graphite electrodes in the half-cell. (c) Charge voltage profiles of C-LFP and R-LFP at 1 mA tested in the electrolytic cell. (d) X-ray diffraction (XRD) patterns of LFP before and after repair.

On the other hand, Li lost from the degraded cathode actually exists in the graphite anode in the inactive form of the SEI, dead Li, and trapped Li.[23−25] Recently, some work has been done to extract Li from the degraded anode to regenerate the degraded cathode,[26,27] which successfully improves the recovery efficiency but requires additional tedious processes. Therefore, if residual Li on the graphite surface can be directly converted into Li^+ and can refill Li vacancies in degraded LFP, it will greatly shorten and simplify the repair process and improve its usability. Dead Li restoration has been proven viable,[24,28] demonstrating that inactive components can be converted to active Li to prolong the lifespan of Li metal batteries. However, rejuvenating SEIs in LIBs has received little attention.

In this work, built on the existing knowledge of the LFP battery failure mechanism, we proposed to use accumulated inactive Li in the SEI as a Li source to supplement the Li loss in degraded LFP through activation via deep discharge. In the electrochemical process, the electrons released by the SEI create the reductive environment to restore Fe(III) to Fe(II) and eliminate antisite defects. Under the multiple effects of the SEI, we achieved cell repair without external additives and with no need for damage to the cell integrity. This repair strategy has been validated by pouch cells, which show significant capacity enhancement and resistance reduction. Benefiting from it, the repaired cell shows a better cycling stability, with 50% more cycles than the degraded cell for the same 4% capacity decay and an extended cycle life of over 274 cycles at 1 C. This facile strategy can be reused repeatedly to maximize its potential for extending the service life of degraded cells, making them valuable for practical industry adoption.

RESULTS AND DISCUSSION

Design Concept of the Repair Strategy Based on Deep Discharge. The SEI has a complex composition, typically containing inorganic compounds (e.g., LiF, Li_2CO_3) and organic components (e.g., various lithium alkyl carbonates and polymeric species).[29,30] Compared with the extensive focus on SEI formation and evolution,[31,32] a very few works have discussed the electrochemical behavior of the SEI beyond the conventional operating voltage range. During deep discharge, the electrochemical potential of the anode (μ_A) gradually decreases, that is, the anodic potential gradually increases (Figure 1a). If μ_A' is below the highest occupied molecular orbital (HOMO) energy of the SEI, it will oxidize the SEI and release electrons. Part of the organic components in the SEI (e.g., lithium ethylene decarbonate (LEDC)) have relatively low oxidation potentials (high HOMO energy), while components like LiF, Li_2CO_3, and polymeric species are more difficult to oxidize (Table S1, Supporting Information). Different capabilities of losing electrons enable the SEI to selectively decompose through the control of the anodic potential. While unstable organic components decompose by anodic potential elevation, inorganic and polymeric species

https://doi.org/10.1021/acsnano.4c03221
ACS Nano 2024, 18, 21125−21134

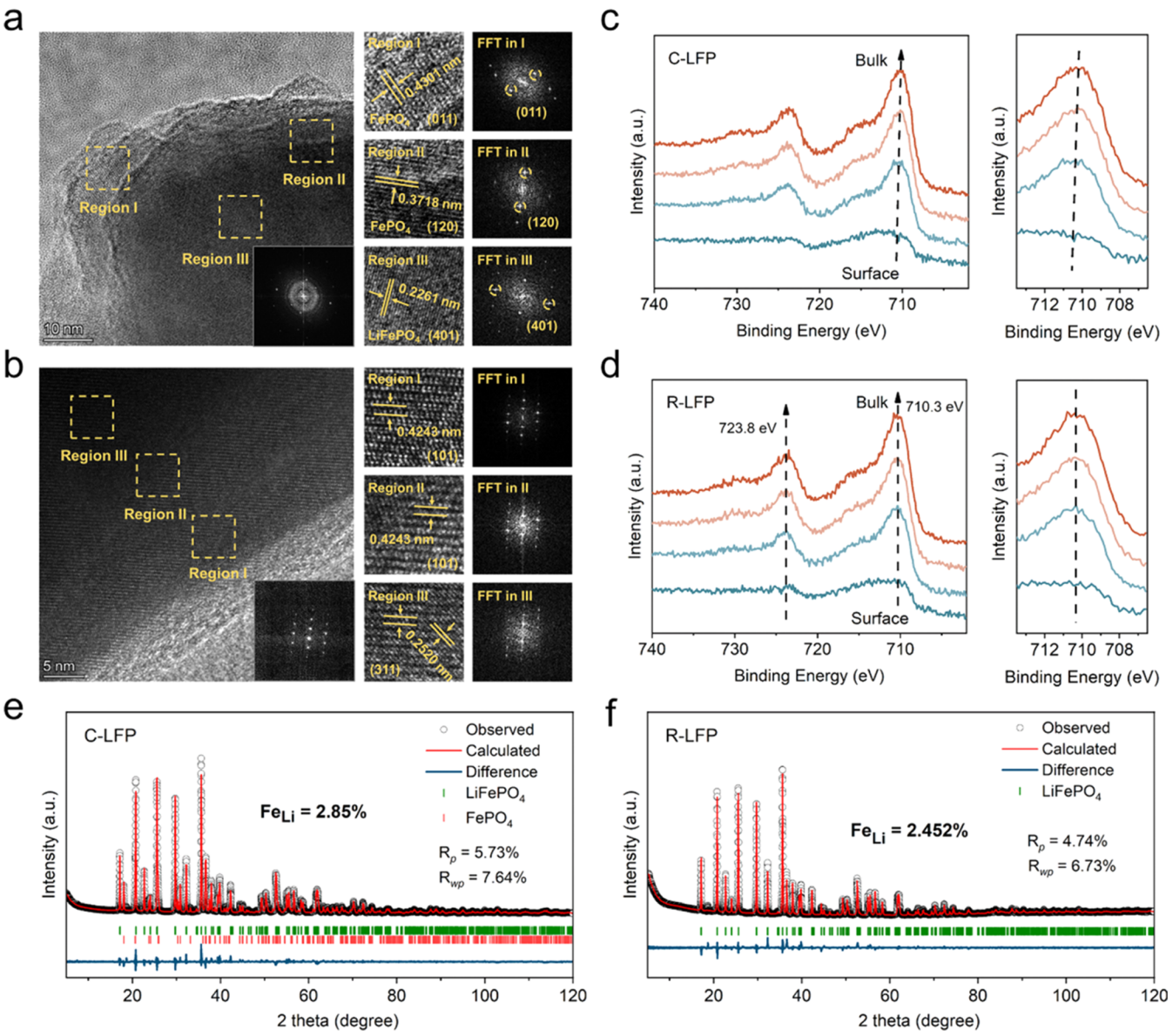

Figure 2. Phase structure characterization of LFP from a holistic and microscopic point of view. HRTEM image of (a) C-LFP and (b) R-LFP and the corresponding FFT patterns. Fe 2p XPS spectra of (c) C-LFP and (d) R-LFP. Rietveld refinement results of (e) C-LFP and (f) R-LFP.

with good mechanical properties[33] and electronic insulation[34] can be retained to ensure the stability of the anode/electrolyte interface. On the cathode side, the degraded LFP electrode will receive the same amount of e^- and Li^+ transported from the anode via the circuit and electrolyte, contributing to Fe(III) reduction and Li replenishment. In short, the repair strategy involves two parallel processes: decomposition of the SEI with an elevated anodic potential and repair of degraded LFP.

The electrolytic cell was introduced to better determine electrochemical behaviors on the cathode and anode sides during deep discharge (Figure S1, Supporting Information). Cycled LFP (C-LFP) was assembled as the working electrode, while sufficient cycled graphite (C-Graphite) in a delithiated state and lithium foil served as the counter electrode and the reference electrode, respectively. Excess C-Graphite was used to fully meet the needs of C-LFP repair. Simple characterizations tentatively confirmed changes in the C-Graphite and C-LFP electrodes. After deep discharge, the typical semicircle corresponding to R_{ct} and R_{SEI} disappeared in the electrochemical impedance spectroscopy (EIS) of graphite with the potential raised to 3.4 V (HP-Graphite) (Figure 1b), implying that the dense SEI layer formed on C-Graphite had been destroyed. Subsequently, the capacity of degraded LFP before and after deep discharge was compared by a galvanostatic charge at 1 mA. The significant enhancement in the capacity of repaired LFP (R-LFP) indicates that a great deal of Li was replenished into the LFP lattice during the process (Figure 1c). In addition, the charge voltage plateau of R-LFP also slightly decreased, demonstrating the improved kinetics of R-LFP. The structural changes of both LFP and graphite were further observed by X-ray diffraction (XRD). R-LFP became a single LFP phase with no FP phase signal observed, suggesting the complete repair of R-LFP (Figure 1d). Moreover, deep discharge did not cause structural damage or impurity formation for both LFP and graphite (Figure S2, Supporting

https://doi.org/10.1021/acsnano.4c03221
ACS Nano 2024, 18, 21125−21134

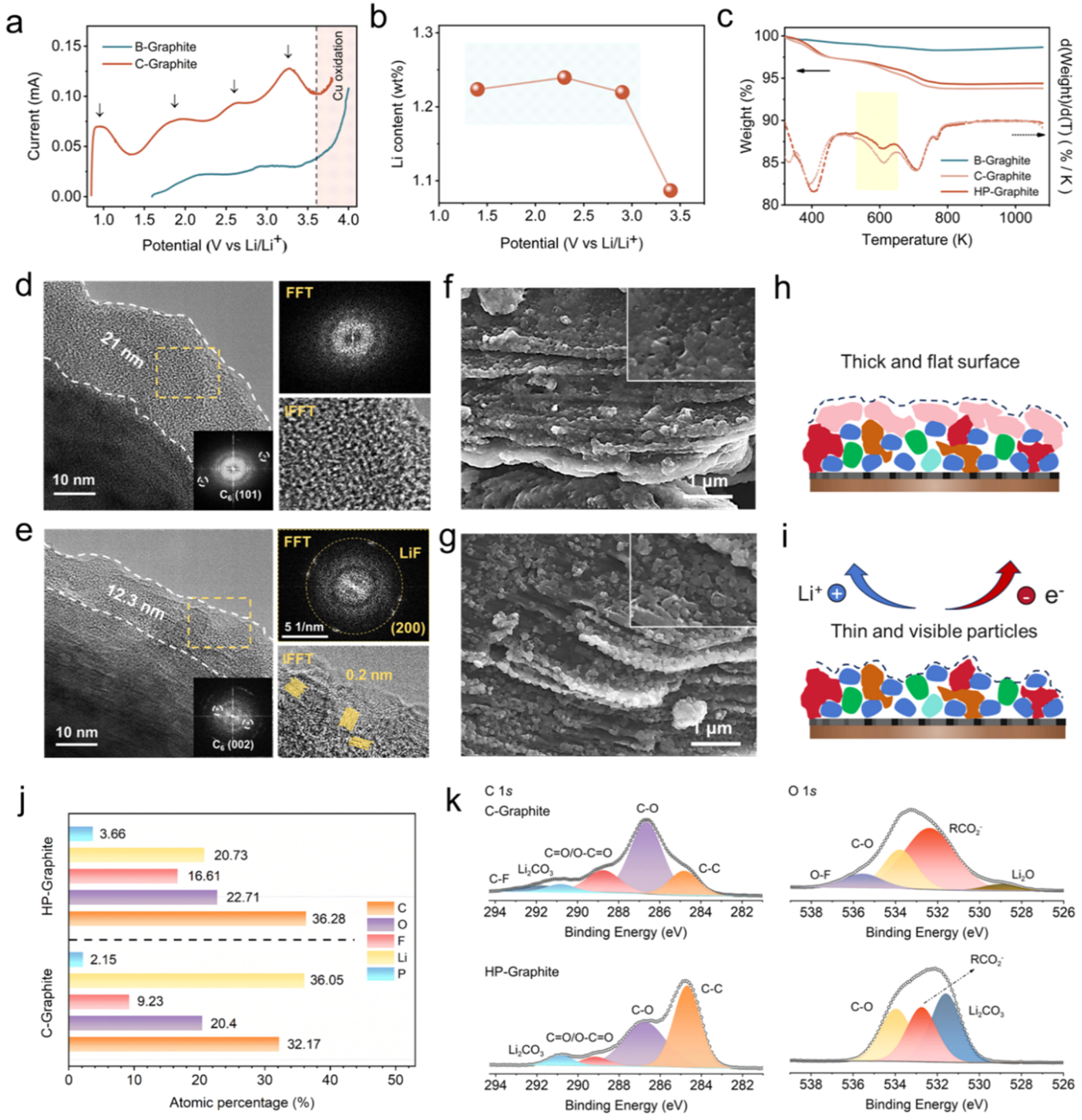

Figure 3. Evolution of graphite during deep discharge. (a) LSV curves of B-Graphite and C-Graphite at a scanning rate of 1 mV s^{-1}. (b) Changes in the Li content with increasing potentials. (c) TG analysis of B-Graphite, C-Graphite, and HP-Graphite under an argon atmosphere. HRTEM image of the SEI and the corresponding FFT image of (d) C-Graphite and (e) HP-Graphite. SEM images of (f) C-Graphite and (g) HP-Graphite. Schematic evolution of the SEI on (h) C-Graphite and (i) HP-Graphite. (j) Relative elemental content of C-Graphite and HP-Graphite. (k) XPS analysis of C 1s and O 1s for C-Graphite and HP-Graphite.

Information). Hence, simultaneous SEI breakdown and C-LFP repair can be achieved during deep discharge.

However, there are still some issues to be noticed and explored. For example, can C-LFP be repaired evenly without microscopic damage? Which provides Li^+ for C-LFP, the electrolyte, or the SEI? How does the SEI change as the potential rises? Some works regarded deep discharge as a destructive behavior detrimental to cell stability,[35,36] so the question arises whether the repaired cells can cycle stably and maintain their repair effects in the long term? These issues will be discussed in the following sections.

Feasibility Assessment of the Regeneration of Degraded LFP Electrodes. To verify the viability of directly regenerating C-LFP based on deep discharge, the phase structures of both C-LFP and R-LFP were analyzed from a holistic and microscopic point of view. As shown in Figure 2a, the fast Fourier transform (FFT) image of C-LFP displays an irregular arrangement. Subsequently, three distinct regions in

https://doi.org/10.1021/acsnano.4c03221
ACS Nano 2024, 18, 21125−21134

the high-resolution transmission electron microscope (HRTEM) image were selected for microscopic phase structure analysis. All three areas show different lattice fringes and FFT images. Region I and II near the edges of the particle display a lattice spacing of 0.4301 and 0.3718 nm, respectively, corresponding to the (011) and (120) planes of FP, while in region III, which is closer to the interior of the particle, the (401) plane of LFP is detected with a lattice spacing of 0.2261 nm. Besides, some diffraction spots of the FP phase also exist in the FFT image of region III, which indicates that the FP and LFP phases coexist. In contrast, as to R-LFP, the three regions selected from the surface to the interior exhibit the same FFT image and the same lattice spacing of 0.4243 and 0.2520 nm, ascribed to the (101) and (311) planes of LFP, respectively (Figure 2b). R-LFP has a uniform and single-phase distribution. Depth etching X-ray photoelectron spectroscopy (XPS) was further adopted to analyze the valence changes of Fe. To avoid interfering with the results, no treatment was done on the sample surface, and both C-LFP and R-LFP initially exhibited indistinguishable Fe peaks due to surface coverings (Figures S3 and S4, Supporting Information). For C-LFP, with an increasing etching depth, the Fe $2p_{3/2}$ peak at ~710 eV shifts gradually to a lower binding energy, suggesting a gradual change in the valence state of Fe from the surface to the bulk (Figure 2c). Combined with HRTEM results (Figure 2a,b), the higher binding energy near the surface is attributed to the more Li-deficient Fe(III) phase.[37] For R-LFP, the Fe $2p_{3/2}$ peak at 710.3 eV and the Fe $2p_{1/2}$ peak at 723.8 eV remain unchanged (Figure 2d), indicating that the Fe(III) phase near the surface disappears after repair. Except for phase recovery, the antisite defect is also a significant parameter for LFP evaluation. According to the Rietveld refinement results calculated from XRD, the defect value was reduced from 2.85 (Figure 2e; Table S2, Supporting Information) to 2.452% (Figure 2f; Table S3, Supporting Information). Reducing antisite defects is vital for improving Li^+ diffusion,[38] consistent with the lower charge voltage plateau exhibited by R-LFP, as shown in Figure 1c. C-LFP requires a higher overpotential to overcome the impediment due to defects obstructing Li^+ diffusion channels, while the extra electrons R-LFP gained from the anode side can reduce Fe^{3+}, thereby leading to a decrease in the activation barrier of cation migration, thus reordering the transport channels for better Li^+ diffusion.[17] The morphologies of C-LFP and R-LFP were also observed by scanning electron microscopy (SEM) and energy-dispersive spectroscopy (EDS) mapping (Figures S5 and S6, Supporting Information). No obvious cracks on the LFP electrode could be observed, and the surface remained smooth and dense without the appearance of any deposit, implying that replenished Li^+ was allocated to the relevant Li layer in the octahedral structure without structural damage.[39] In short, direct regeneration based on deep discharge enables uniform Li replenishment and defect elimination, demonstrating the feasibility of this strategy for repairing the C-LFP electrode.

For repairing degraded LFP, both Fe(III) reduction and adequate Li replenishment are indispensable elements. During deep discharge, Fe(III) can easily obtain electrons for reduction due to the release of electrons from the oxidative decomposition of the SEI. However, the source of Li replenished by R-LFP deserves further investigation. Inductively coupled plasma optical emission spectroscopy (ICP-OES) data (Table S4, Supporting Information) reveal that the Li content in graphite significantly decreased from 1.304 to 0.994% after deep discharge, indicating that about 24% of inactive Li was released from graphite. While C-Graphite was only soaked in the electrolyte for 30 h, its Li content remained almost unchanged (Figure S7a, Supporting Information), and the ^1H nuclear magnetic resonance (NMR) confirms that no new peak is found (Figure S7b, Supporting Information), denying the Li loss of HP-Graphite due to SEI dissolution in the electrolyte. As a result, it can be assumed that the decrease of the Li content in HP-Graphite is not a time-dependent process, but is related to the electrochemical reactions involved in the deep discharge process. Li lost in HP-Graphite may be released directly in the form of Li^+ alone or as soluble Li-containing products from the oxidation reaction, which would eventually exist in the electrolyte in the form of solvated Li^+. Hence, C-Graphite can act as both an e^- and Li^+ donor to promote the recovery of C-LFP.

Evolution of Graphite During Deep Discharge. The evolution of C-Graphite during deep discharge was further analyzed to gain insight into the repair mechanism. Figure 3a exhibits the oxidation reactions as the anodic potential rises at a 1 mV s^{-1} scanning rate, and bare graphite (B-Graphite) without being cycled was used as a control. The linear sweep voltammetry (LSV) curves of both B-Graphite and C-Graphite show a rapid increase in current when the potential reaches about 3.5 V, indicating the oxidation of the Cu collector, which needs to be avoided.[35,39] Four peaks appearing in the C-Graphite curve before 3.5 V demonstrate that the SEI underwent oxidation reactions, which is not found in B-Graphite. Surprisingly, only when the anodic potential rises above 2.9 V does the Li content in C-Graphite decrease significantly (Figure 3b and the detailed data are supplied in Table S5, Supporting Information), which indicates that the SEI does not release Li^+ until above 2.9 V. Considering the significant capacity release before reaching 2.9 V (Figure S8, Supporting Information), it can be assumed that a series of conversion reactions without releasing Li^+ occurs in the SEI below 2.9 V. And the electrolyte provides Li^+ to realize a closed circuit in this process, which means that a part of Li replenished in degraded LFP comes from the electrolyte. The thermogravimetry (TG) analysis, as shown in Figure 3c, further confirms the weight loss of HP-Graphite. Since the inorganic components of the SEI (e.g., LiF, Li_2CO_3) have decomposition temperatures of up to 900 K,[26] the less weight loss of HP-Graphite around 600 K (Figure S9, Supporting Information) can be attributed to the decomposition of organic components of the SEI.

Subsequently, the SEI on the graphite anode was directly observed using HRTEM. The apparent contrast in the shades can clearly distinguish the SEI region. The thickness of the SEI on HP-Graphite is 12.3 nm (Figure 3e), much smaller than that on C-Graphite (Figure 3d). Notably, the SEI on C-Graphite shows a distinct amorphous phase corresponding to the diffuse ring in FFT. Different from C-Graphite, the HP-Graphite SEI contains lattice characteristics embedded in the amorphous matrix and the lattice spacing is about 0.2 nm, representing the (200) plane of LiF. Then, clear areas of stacked graphite flakes were selected for SEM analysis. C-Graphite shows a relatively flat surface with slight unevenness (Figure 3f), whereas the HP-Graphite surface appears to have many small and well-defined particles (Figure 3g). The elemental distribution was detected by EDS (Figure S10, Supporting Information). Both the F and the O elements are concentrated at the edges of graphite layers, where particles are

https://doi.org/10.1021/acsnano.4c03221
ACS Nano 2024, 18, 21125−21134

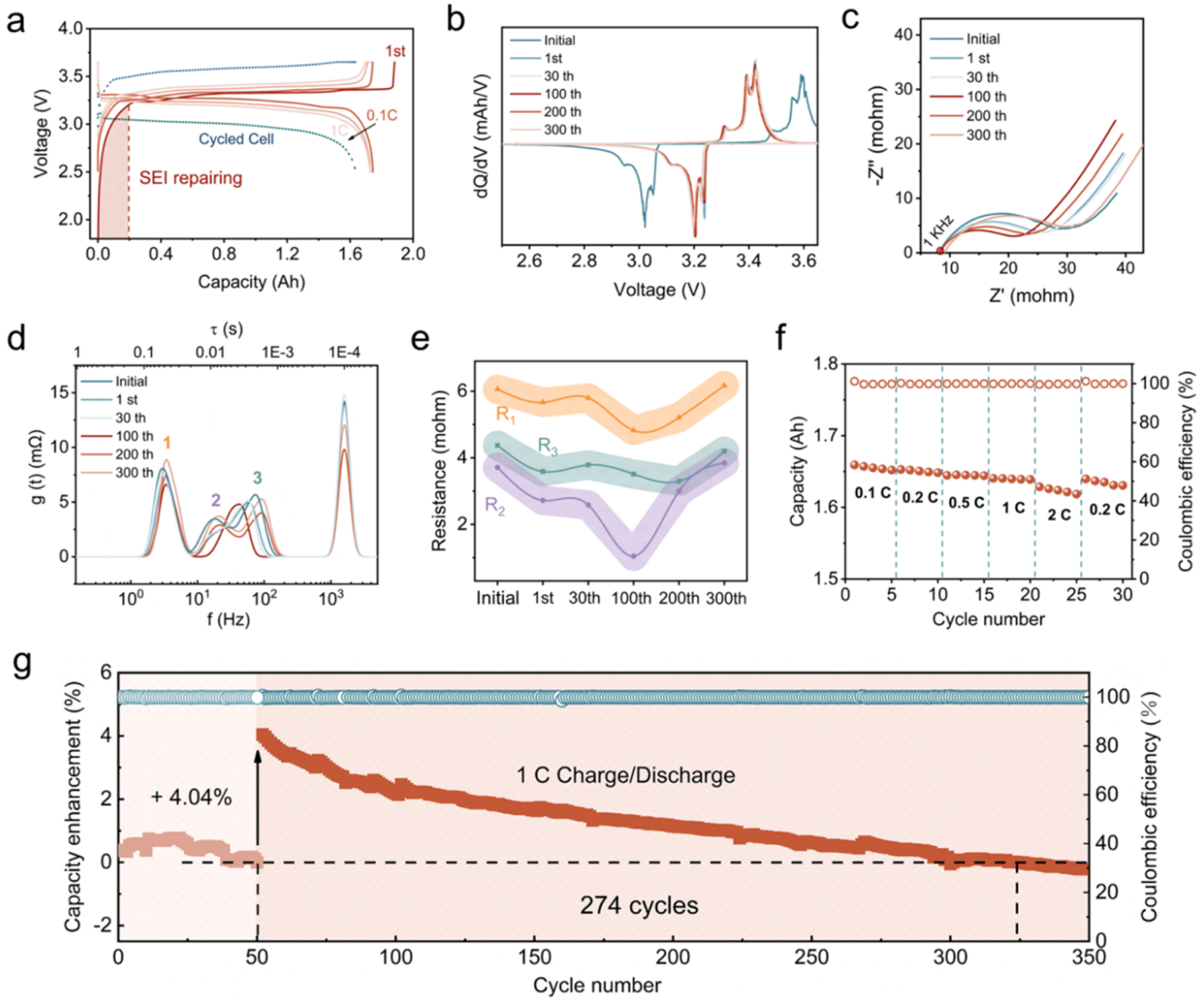

Figure 4. Electrochemical evaluation of the repair strategy. (a) Galvanostatic charge/discharge profiles of the C-Cell at 1 C (dashed line) and the R-Cell at 0.1, 0.5, and 1 C (colors from dark to light). (b) Differential capacity analysis of the C-Cell and the R-Cell at 1 C after different cycles. (c) EIS spectra of the C-Cell (initial) and the R-Cell with different numbers of cycles. (d) DRT spectra transformation of the EIS spectra. (e) Resistance changes corresponding to three peaks in the frequency range of 1000−1 Hz. (f) Rate performance of the R-Cell. (g) Cycling performance of the R-Cell at 1 C (the light color shows cycles of the C-Cell and the dark color corresponds to the R-Cell).

rich, revealing that the small particles on the HP-Graphite surface may be LiF. Interestingly, though HP-Graphite seems to have more abundant LiF, C-Graphite and HP-Graphite actually have a similar F atom content, implying that LiF on HP-Graphite is more visible, not more abundant (Figure 3h,i).

A detailed analysis of the surface chemistry of C-Graphite and HP-Graphite by XPS was used to further determine the compositional changes of the SEI. As expected, the F content of HP-Graphite is significantly higher compared to that of C-Graphite due to more inner LiF grains exposed on the surface (Figure 3j). In addition, HP-Graphite has a considerably lower Li content, suggesting that more Li-free components are also exposed on the surface, such as graphite and polymeric species in the SEI. Subsequently, fine scans were conducted in the binding energy regions associated with each element (Figures 3k and S11, Supporting Information). The 286.8 and 289.0 eV peaks in C 1s spectra can be assigned to the carbon atom bound to one and three oxygens, respectively, corresponding to ether and carbonate groups.[40] Such carbonate products may be lithium alkyl carbonates ($ROCO_2Li$) or polycarbonates ($ROCO_2R'$). This assignment is supported by peaks at ~532.5 and 534 eV in the 1*s* spectra, which can be attributed to carbonyl oxygen and oxygen bound to the alkyl group. In addition, the peak at 290.8 eV in the C 1s spectra and 531.6 eV in O 1s together demonstrate the presence of inorganic Li_2CO_3. After deep discharge, the 286.8 eV peak in C 1s and the 532.5 eV peak in O 1s corresponding to carbonate groups are significantly weaker, suggesting that $ROCO_2Li$ decomposed at a high potential. Meanwhile, the content of Li_2CO_3 elevates apparently, which may be due to a greater exposure in the absence of an organic layer or from the transformation of $ROCO_2Li$.

All of these characterizations reveal that at a high potential, the unstable organic component $ROCO_2Li$ in the outer layer of the SEI decomposes, while the stable inorganic components and polymeric species in the inner layer are retained. Without

https://doi.org/10.1021/acsnano.4c03221
ACS Nano 2024, 18, 21125−21134

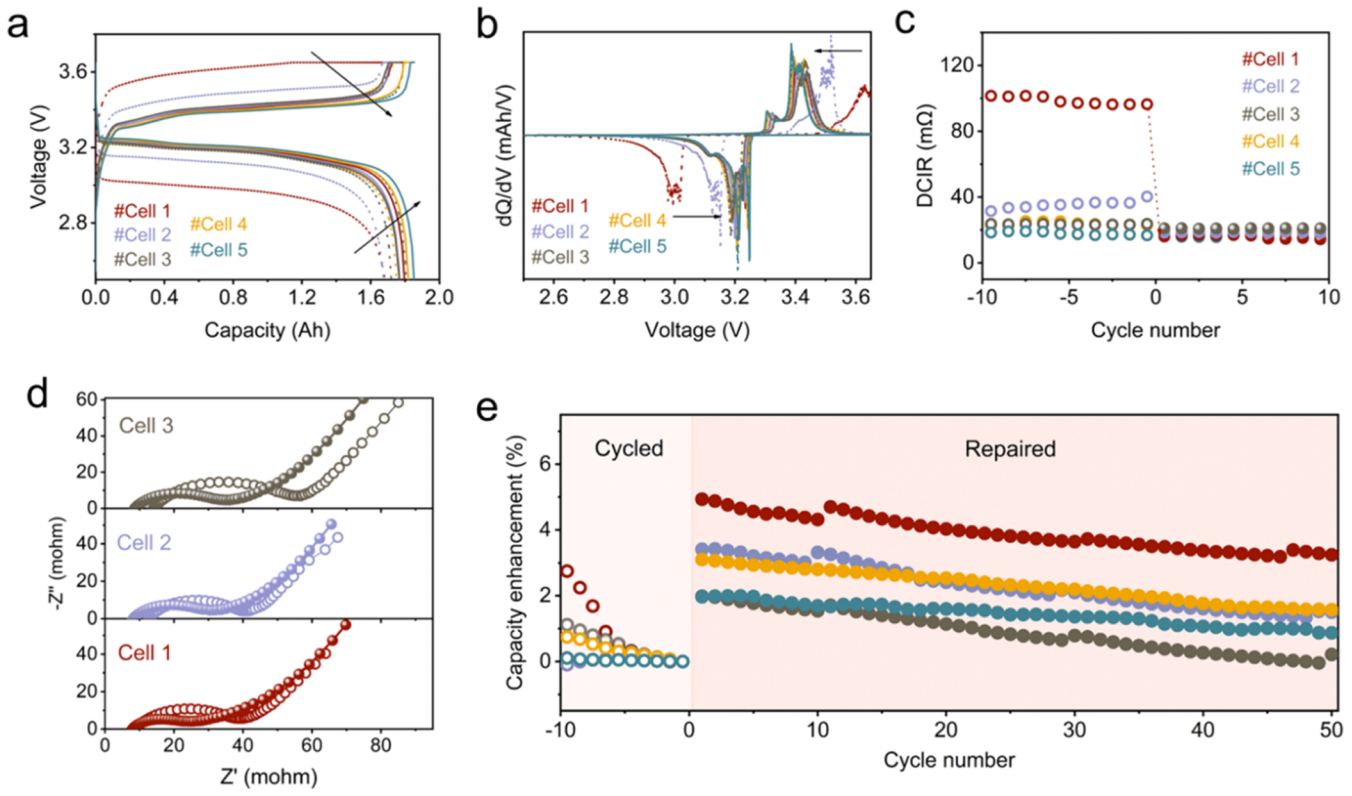

Figure 5. Electrochemical evaluation of the repair effectiveness of different cells. (a) Galvanostatic charge/discharge profiles of cells before (dashed lines) and after (solid lines) repair at 1 C. (b) Differential capacity analysis of cells before (dashed lines) and after (solid lines) repair. (c) Changes in the DC internal resistance of cells before (hollowed) and after (solid) repair. (d) EIS spectra of cells before repair (hollowed) and 50 cycles after repair (solid). (e) Cyclic performance of R-Cells at 1 C.

the cover of the outer organic component, more inorganic components hidden under it are exposed to the surface.

Electrochemical Evaluation of Cell Repair. We have demonstrated that the SEI on the surface of C-Graphite partially decomposes and thins by deep discharge, while C-LFP receives both e^- and Li^+ to complete its repair process. The process does not require any external additives, making closed-loop and nondisassembly repair for complete cells possible.

Herein, the feasibility of cell repair based on deep discharge was demonstrated by 2.3 Ah graphite||LFP pouch cells (see Figure S12 for detailed parameters of pouch cells), which had been cycled thousands of times with >20% capacity decay. Cycled cell (C-cell) delivered a discharge capacity of 1.63 Ah at 1 C and exhibited severe polarization (Figure 4a). After deep discharge, we used low-current charging for the first cycle to repair the possible voids in the SEI in the decomposition process. The charge capacity of the first cycle was 1.88 Ah at 0.05 C, which indicates that about 37% of lost Li was replenished back into C-LFP, resulting in an increase of the R-Cell capacity by 10.87% compared to the original C-Cell. Notably, compared to the C-Cell with an onset charge voltage of 2.8 V, the start voltage of the R-Cell was much lower in its first charge. The R-Cell had released quite a bit of capacity before reaching its voltage plateau, suggesting that a part of restored Li was reused to repair the destroyed SEI. Similarly, the small peak at ~2.4 V observed in its corresponding differential capacity analysis (dQ/dV) curve further confirmed new SEI regeneration (Figure S13, Supporting Information). Even so, the R-Cell still delivered an improved capacity of 1.75 Ah in the subsequent 0.1 C cycle, and its capacity decay was negligible with the gradual increase of the charge/discharge rate from 0.1 to 1 C. Furthermore, the dQ/dV curves also demonstrated the improved reaction kinetics of the R-Cell (Figure 4b). The R-cell showed a stable charge/discharge voltage platform with an overvoltage of about 0.2 V, much lower than the C-Cell. After 300 cycles, the low overvoltage could still be maintained. Likewise, the resistance of the R-Cell was significantly reduced (Figure 4c). On the other hand, the reappearance of the semicircle in the R-Cell also indicated that the repaired SEI had become dense and intact again. Especially after 100 cycles, the semicircle corresponding to R_{ct} and R_{SEI} is almost half the C-Cell. Subsequently, the distribution of relaxation times (DRT) was obtained from EIS spectra to further elucidate the resistance changes of the individual electrochemical processes (Figure 4d). Three peaks at frequencies lower than 1 kHz were the fitting result of a semicircle, which were further analyzed by calculating their respective impedances (Figure 4e). The first peak in the lower frequency region from 10 to 1 Hz and the second in the middle-frequency region from 100 to 10 Hz represent the charge transfer and SEI layer at the anode.[41,42] After deep discharge, the resistance values R_1 and R_2 corresponding to these two peaks showed the same trend, both reaching their lowest values at the 100th cycle; especially, R_2 decreased even more significantly. The lowering of R_{ct} and R_{SEI} in the first 100 cycles suggests a gradual evolution of the SEI to form a stable interface favorable for Li^+ transport. In contrast, R_3 exhibited a limited change, which may stand for the resistance of charge transfer at the cathode.[43] Benefiting from improved kinetics, the R-Cell showed an excellent rate performance, as expected, with a negligible change in the capacity at different rates (Figure 4f). Subsequently, the cycle stability of the R-Cell was

https://doi.org/10.1021/acsnano.4c03221
ACS Nano 2024, 18, 21125−21134

tested, and the stable cycling for 300 cycles at 1 C further proves the reliability of cell repair. The R-Cell with activation exhibits an extended cycle life of more than 274 cycles (Figure 4g). Surprisingly, the R-Cell also showed a better cycling stability after repair, with approximately 50% more cycles compared with the C-Cell at the same capacity loss (Figure S14, Supporting Information). In the first 100 cycles, the SEI of the R-Cell still evolves, resulting in a faster capacity decay, which is consistent with the trend of the resistance change in EIS spectra. After the stable interface formed, the R-Cell showed a much more stable cycling performance due to better dynamics.

The test results of multiple cells further validate the reliability and applicability of the cell repair. The same repair method was used on five cells with different degrees of degradation. All five cells show an enhanced capacity (Figure 5a), a reduced overvoltage (Figure 5b), and a decreased DC internal resistance (Figure 5c). Interestingly, the characteristics of R-Cells are close to each other, especially the kinetic ones. All cells show an overvoltage of less than 0.2 V and a DC resistance of around 20 mΩ (see Table S6 for detailed information on the cell performance before and after repair). EIS spectra of three cells with severe polarization all showed noticeable resistance reduction (Figure 5d), indicating that the SEI had been thinned and modified. And all five cells exhibited good cycling stability (Figure 5e). Notably, the more severe the polarization of the cell, the more influential the repair is, which confirms the outstanding effect in improving the kinetic performance. The better kinetic performance enables R-Cells to deliver a higher usable capacity, which is conducive to prolonging the service life of the cells. Besides, in terms of Cell 4 and Cell 5, whose dynamics were good intrinsically with negligible improvement, they still delivered a steady capacity enhancement, which suggests that excess Li was replenished during deep discharge. These above results illustrate that both the improved kinetic performance and replenished Li play critical roles in restoring the performance of C-Cells. Furthermore, this repair method can also be applied repeatedly to the same cell after a period of cycling (Figure S15, Supporting Information). Though the capacity enhancement gradually weakened with multiple repetitions due to less accumulation of $ROCO_2Li$, the cell still showed an impressive life extension at each repair. The feasibility of repetitive repairs makes its unlimited potential extend the service life of cells, showing great practical application value.

CONCLUSIONS

In summary, we put forward a strategy to rejuvenate the inactive organic components in the SEI via deep discharge, by which we successfully realize cell repair. With the aid of multiple characterizations and electrochemical evaluations, the electrochemical behavior occurring on the cathode and anode sides during deep discharge was comprehensively analyzed, and their mechanisms were explained in detail. The results showed that the core of repair lies in the oxidative decomposition of the SEI, which exhibits three effects: (1) The SEI acts as a lithium source to replenish the composition for C-LFP. (2) The SEI provides excess electrons to reduce Fe^{3+}, thereby reducing the activation barrier of recombining "antisite" defects. (3) The thinning and modification of the SEI through decomposition and regeneration improve the dynamics of R-Cells, improving their cycling stability and allowing more available capacity to be utilized. Unlike previous recycling efforts, the restoration of degraded cells is entirely attributed to their internal supply without destroying the integrity of cells, which provides opportunities for extending the service life and promoting the secondary use of spent cells. In addition, we provide not only a strategy for repairing degraded LFP cells but also an insight into the electrochemical evolution of the SEI beyond the operating voltage range of cells.

METHODS

Regeneration of Degraded LFP Electrodes. Direct regeneration of degraded LFP electrodes was carried out in an electrolytic cell. First, the degraded pouch cells in the discharged state were manually dismantled in the glovebox filled with Ar. After being rinsed with dimethyl carbonate (DMC), cycled electrodes were obtained. Then, these cut electrodes were assembled into a three-electrode system, in which cycled LFP was the working electrode, and cycled graphite in a delithiated state and lithium foil served as the counter electrode and the reference electrode, respectively. Excess graphite was used to fully meet the needs of degraded LFP repair, and its delithiated state ensured that this regeneration process was entirely based on the electrochemical behavior of the SEI. After assembly, the working electrodes were discharged to 2.5 V vs Li/Li^+ at 0.1 mA, by which LFP electrodes could replenish Li until Li vacancies were completely filled.

Repair of Degraded LFP Cells. The degraded pouch cells in the discharged state were further deeply discharged at a rate of 0.1 C or less. Subsequently, the cells were recharged at 0.05 C to repair the damaged SEI and then placed in a thermostat at 45 °C for 24 h.

Material Characterization. XRD patterns were collected using a Bruker D8 Venture diffractometer for phase analysis and defect calculation. The microstructure of LFP and the SEI on graphite were observed by TEM (Talos F200X G2, America). SEM (JEOL JSM-7800F, China), along with EDS, was employed to detect the morphology and elemental distribution of the electrodes. XPS spectra for valence analysis and surface chemistry were tested on a Thermo Scientific ESCALAB Xi+ photoelectron spectrometer. The accurate elemental contents were obtained by ICP-OES (PerkinElmer Avio500, Singapore). TG was applied to compare the weight loss of graphite anodes in different states at a 10 °C min^{-1} heating rate up to 800 °C in an argon atmosphere. ^1H NMR spectra were obtained using a Bruker Avance III spectrometer with deuterated dimethyl sulfoxide as the solvent.

Electrochemical Measurements. The electrochemical tests of graphite electrodes were carried out in coin-type half-cells with Li metal foils as counter electrodes. As for LFP electrodes, their galvanostatic charging tests were performed in a three-electrode system. For both systems, the electrolyte used was 1 M lithium hexafluorophosphate ($LiPF_6$) in the mixture of ethylene carbonate (EC)/DMC/ethyl methyl carbonate (EMC) (1:1:1 by volume). In terms of degraded LFP cells, assembly is not required, as no disassembly is conducted. The electrochemical performance of cells was measured within the voltage range of 2.5−3.65 V at 30 °C.

ASSOCIATED CONTENT

Supporting Information

The Supporting Information is available free of charge at https://pubs.acs.org/doi/10.1021/acsnano.4c03221.

More structural characterizations, compositional information, electrochemical measurements, and supplementary data tables (PDF)

AUTHOR INFORMATION

Corresponding Authors

Yumeng Zhao − *Key Laboratory for Green Chemical Technology of Ministry of Education, School of Chemical*

https://doi.org/10.1021/acsnano.4c03221
ACS Nano 2024, 18, 21125−21134

Engineering and Technology, Tianjin University, Tianjin 300072, China; Email: yumengzhao@tju.edu.cn

Jiayan Luo − *State Key Laboratory of Metal Matrix Composites, School of Materials Science and Engineering, Shanghai Jiao Tong University, Shanghai 200240, China; Zhang jiang Institute for Advanced Study, Shanghai Jiao Tong University, Shanghai 200240, China; Shanghai Jiao Tong University Shaoxing Research Institute of Renewable Energy and Molecular Engineering, Shaoxing 312000, China;* orcid.org/0000-0002-4619-6040; Email: jyluo@sjtu.edu.cn

Authors

Xiaodi Zhao − *State Key Laboratory of Metal Matrix Composites, School of Materials Science and Engineering, Shanghai Jiao Tong University, Shanghai 200240, China*

Hao Chen − *State Key Laboratory of Metal Matrix Composites, School of Materials Science and Engineering, Shanghai Jiao Tong University, Shanghai 200240, China*

Hu Wu − *State Key Laboratory of Metal Matrix Composites, School of Materials Science and Engineering, Shanghai Jiao Tong University, Shanghai 200240, China*

Complete contact information is available at: https://pubs.acs.org/10.1021/acsnano.4c03221

Author Contributions

X.Z., Y.Z., and J.L. conceived and designed this work. X.Z. performed the experiments, analyzed data, and wrote the original draft. H.C. and H.W. aided in experiments. All authors have given support to the final version of the manuscript.

Notes

The authors declare no competing financial interest.

ACKNOWLEDGMENTS

The authors acknowledge the financial support from the start-up fund of Shanghai Jiao Tong University and the Open Foundation of the Shanghai Jiao Tong University Shaoxing Research Institute of Renewable Energy and Molecular Engineering (Grant number: JDSX2022023).

REFERENCES

(1) Li, J. K.; Ma, Z. F. Past and Present of $LiFePO_4$: From Fundamental Research to Industrial Applications. *Chem* **2019**, *5*, 3−6.

(2) Fan, E. S.; Li, L.; Wang, Z. P.; Lin, J.; Huang, Y. X.; Yao, Y.; Chen, R. J.; Wu, F. Sustainable Recycling Technology for Li-Ion Batteries and Beyond: Challenges and Future Prospects. *Chem. Rev.* **2020**, *120*, 7020−7063.

(3) Chen, M. Y.; Ma, X. T.; Chen, B.; Arsenault, R.; Karlson, P.; Simon, N.; Wang, Y. Recycling End-of-Life Electric Vehicle Lithium-Ion Batteries. *Joule* **2019**, *3*, 2622−2646.

(4) Yu, X. L.; Li, W. K.; Gupta, V.; Gao, H. P.; Tran, D.; Sarwar, S.; Chen, Z. Current Challenges in Efficient Lithium-Ion Batteries' Recycling: A Perspective. *Global Challenges* **2022**, *6*, No. 2200099.

(5) Shi, Y.; Chen, G.; Liu, F.; Yue, X. J.; Chen, Z. Resolving the Compositional and Structural Defects of Degraded $LiNi_xCo_yMn_zO_2$ Particles to Directly Regenerate High-Performance Lithium-Ion Battery Cathodes. *ACS Energy Lett.* **2018**, *3*, 1683−1692.

(6) Xu, P. P.; Dai, Q.; Gao, H. P.; Liu, H. D.; Zhang, M. H.; Li, M. Q.; Chen, Y.; An, K.; Meng, Y. S.; Liu, P.; Li, Y. R.; Spangenberger, J. S.; Gaines, L.; Lu, J.; Chen, Z. Efficient Direct Recycling of Lithium-Ion Battery Cathodes by Targeted Healing. *Joule* **2020**, *4*, 2609−2626.

(7) Ji, G. J.; Wang, J. X.; Liang, Z.; Jia, K.; Ma, J.; Zhuang, Z. F.; Zhou, G. M.; Cheng, H. M. Direct Regeneration of Degraded Lithium-Ion Battery Cathodes with A Multifunctional Organic Lithium Salt. *Nat. Commun.* **2023**, *14*, No. 584.

(8) Gupta, V.; Appleberry, M.; Li, W. K.; Chen, Z. Direct Recycling Industrialization of Li-Ion Batteries: The Pre-Processing Barricade. *Next Energy* **2024**, *2*, No. 100091.

(9) Zhao, Y. Y.; Pohl, O.; Bhatt, A. I.; Collis, G. E.; Mahon, P. J.; Ruther, T.; Hollenkamp, A. F. A Review on Battery Market Trends, Second-Life Reuse, and Recycling. *Sustainable Chem.* **2021**, *2*, 167−205.

(10) Gupta, V.; Yu, X. L.; Gao, H. P.; Brooks, C.; Li, W. K.; Chen, Z. Scalable Direct Recycling of Cathode Black Mass from Spent Lithium-Ion Batteries. *Adv. Energy Mater.* **2023**, *13*, No. 2203093.

(11) Chen, S.; He, T.; Lu, Y.; Su, Y. F.; Tian, J.; Li, N.; Chen, G.; Bao, L. Y.; Wu, F. Renovation of $LiCoO_2$ with Outstanding Cycling Stability by Thermal Treatment with Li_2CO_3 from Spent Li-Ion Batteries. *J. Energy Storage* **2016**, *8*, 262−273.

(12) Zhang, N.; Stark, J.; Li, H. Y.; Liu, A. R.; Li, Y.; Hamam, I.; Dahn, J. R. Effects of Fluorine Doping on Nickel-Rich Positive Electrode Materials for Lithium-Ion Batteries. *J. Electrochem. Soc.* **2020**, *167*, No. 080518.

(13) Zheng, Y. D.; Zhang, R. H.; Vanaphuti, P.; Liu, Y. T.; Yang, Z. Z.; Wang, Y. Positive Role of Fluorine Impurity in Recovered $LiNi_{0.6}Co_{0.2}Mn_{0.2}O_2$ Cathode Materials. *ACS Appl. Mater. Interfaces* **2021**, *13*, 57171−57181.

(14) Kobayashi, S.; Kuwabara, A.; Fisher, C. A. J.; Ikuhara, Y. Atomic-Scale Analysis of Biphasic Boundaries in the Lithium-Ion Battery Cathode Material $LiFePO_4$. *ACS Appl. Energy Mater.* **2020**, *3*, 8009−8016.

(15) Kim, J. H.; Woo, S. C.; Park, M. S.; Kim, K. J.; Yim, T.; Kim, J. S.; Kim, Y. J. Capacity Fading Mechanism of $LiFePO_4$-Based Lithium Secondary Batteries for Stationary Energy Storage. *J. Power Sources* **2013**, *229*, 190−197.

(16) Delmas, C.; Maccario, M.; Croguennec, L.; Le Cras, F.; Weill, F. Lithium Deintercalation in $LiFePO_4$ Nanoparticles via A Domino-Cascade Model. *Nat. Mater.* **2008**, *7*, 665−671.

(17) Park, K. Y.; Park, I.; Kim, H.; Lim, H. D.; Hong, J.; Kim, J.; Kang, K. Anti-Site Reordering in $LiFePO_4$: Defect Annihilation on Charge Carrier Injection. *Chem. Mater.* **2014**, *26*, 5345−5351.

(18) Fan, M.; Meng, Q. H.; Chang, X.; Gu, C. F.; Meng, X. H.; Yin, Y. X.; Li, H. L.; Wan, L. J.; Guo, Y. G. In Situ Electrochemical Regeneration of Degraded $LiFePO_4$ Electrode with Functionalized Prelithiation Separator. *Adv. Energy Mater.* **2022**, *12*, No. 2103630.

(19) Wang, T.; Yu, X. S.; Fan, M.; Meng, Q. H.; Xiao, Y.; Yin, Y. X.; Li, H. L.; Guo, Y. G. Direct Regeneration of Spent LiFePO4 via A Graphite Prelithiation Strategy. *Chem. Commun.* **2020**, *56*, 245−248.

(20) Wu, C.; Hu, J. M.; Ye, L.; Su, Z. P.; Fang, X. L.; Zhu, X. L.; Zhuang, L.; Ai, X. P.; Yang, H. X.; Qian, J. F. Direct Regeneration of Spent Li-Ion Battery Cathodes via Chemical Relithiation Reaction. *ACS Sustainable Chem. Eng.* **2021**, *9*, 16384−16393.

(21) Xu, P. P.; Tan, D. H. S.; Jiao, B. L.; Gao, H. P.; Yu, X. L.; Chen, Z. A Materials Perspective on Direct Recycling of Lithium-Ion Batteries: Principles, Challenges and Opportunities. *Adv. Funct. Mater.* **2023**, *33*, No. 2213168.

(22) Ma, J.; Wang, J. X.; Jia, K.; Liang, Z.; Ji, G. J.; Zhuang, Z. F.; Zhou, G. M.; Cheng, H. M. Adaptable Eutectic Salt for the Direct Recycling of Highly Degraded Layer Cathodes. *J. Am. Chem. Soc.* **2022**, *144*, 20306−20314.

(23) An, S. J.; Li, J. L.; Daniel, C.; Mohanty, D.; Nagpure, S.; Wood, D. L. The State of Understanding of the Lithium-Ion-Battery Graphite Solid Electrolyte Interphase (SEI) and Its Relationship to Formation Cycling. *Carbon* **2016**, *105*, 52−76.

(24) Liu, F.; Xu, R.; Wu, Y. C.; Boyle, D. T.; Yang, A. K.; Xu, J. W.; Zhu, Y. Y.; Ye, Y. S.; Yu, Z. A.; Zhang, Z. W.; Xiao, X.; Huang, W. X.; Wang, H. S.; Chen, H.; Cui, Y. Dynamic Spatial Progression of Isolated Lithium during Battery Operations. *Nature* **2021**, *600*, 659−663.

(25) Markey, B.; Zhang, M. H.; Robb, I.; Xu, P. P.; Gao, H. P.; Zhang, D. W.; Holoubek, J.; Xia, D.; Zhao, Y. F.; Guo, J. C.; Cai, M.; Meng, Y. S.; Chen, Z. Effective Upcycling of Graphite Anode: Healing and Doping Enabled Direct Regeneration. *J. Electrochem. Soc.* **2020**, *167*, No. 160511.

(26) Wang, J. X.; Ma, J.; Jia, K.; Liang, Z.; Ji, G. J.; Zhao, Y.; Li, B. H.; Zhou, G. M.; Cheng, H. M. Efficient Extraction of Lithium from Anode for Direct Regeneration of Cathode Materials of Spent Li-Ion Batteries. *ACS Energy Lett.* **2022**, *7*, 2816−2824.
(27) Fan, M.; Chang, X.; Meng, X. H.; Gu, C. F.; Zhang, C. H.; Meng, Q. H.; Wan, L. J.; Guo, Y. G. Structural Restoration of Degraded $LiFePO_4$ Cathode with Enhanced Kinetics Using Residual Lithium in Spent Graphite Anodes. *CCS Chem.* **2023**, *5*, 1189−1201.
(28) Jin, C. B.; Liu, T. F.; Sheng, O. W.; Li, M.; Liu, T. C.; Yuan, Y. F.; Nai, J. W.; Ju, Z. J.; Zhang, W. K.; Liu, Y. J.; Wang, Y.; Lin, Z.; Lu, J.; Tao, X. Y. Rejuvenating Dead Lithium Supply in Lithium Metal Anodes by Iodine Redox. *Nat. Energy* **2021**, *6*, 378−387.
(29) Wang, L. N.; Menakath, A.; Han, F. D.; Wang, Y.; Zavalij, P. Y.; Gaskell, K. J.; Borodino, O.; Iuga, D.; Brown, S. P.; Wang, C. S.; Xu, K.; Eichhorn, B. W. Identifying the Components of the Solid-Electrolyte Interphase in Li-Ion Batteries. *Nat. Chem.* **2019**, *11*, 789−796.
(30) Verma, P.; Maire, P.; Novák, P. A Review of the Features and Analyses of the Solid Electrolyte Interphase in Li-Ion Batteries. *Electrochim. Acta* **2010**, *55*, 6332−6341.
(31) Sun, S. Y.; Yao, N.; Jin, C. B.; Xie, J.; Li, X. Y.; Zhou, M. Y.; Chen, X.; Li, B. Q.; Zhang, X. Q.; Zhang, Q. The Crucial Role of Electrode Potential of a Working Anode in Dictating the Structural Evolution of Solid Electrolyte Interphase. *Angew. Chem., Int. Ed.* **2022**, *61*, No. e202208743.
(32) Heiskanen, S. K.; Kim, J.; Lucht, B. L. Generation and Evolution of the Solid Electrolyte Interphase of Lithium-Ion Batteries. *Joule* **2019**, *3*, 2322−2333.
(33) Tian, Y. F.; Tan, S. J.; Yang, C. P.; Zhao, Y. M.; Xu, D. X.; Lu, Z. Y.; Li, G.; Li, J. Y.; Zhang, X. S.; Zhang, C. H.; Tang, J. L.; Zhao, Y.; Wang, F. Y.; Wen, R.; Xu, Q.; Guo, Y. G. Tailoring Chemical Composition of Solid Electrolyte Interphase by Selective Dissolution for Long-Life Micron-Sized Silicon Anode. *Nat. Commun.* **2023**, *14*, No. 7247.
(34) Lu, Y. Y.; Tu, Z. Y.; Archer, L. A. Stable Lithium Electrodeposition in Liquid and Nanoporous Solid Electrolytes. *Nat. Mater.* **2014**, *13*, 961−969.
(35) Zhou, H. W.; Fear, C.; Jeevarajan, J. A.; Mukherjee, P. P. State-of-Electrode (SOE) Analytics of Lithium-Ion Cells under Over-discharge Extremes. *Energy Storage Mater.* **2023**, *54*, 60−74.
(36) Zheng, Y.; Qian, K.; Luo, D.; Li, Y. Y.; Lu, Q. W.; Li, B. H.; He, Y. B.; Wang, X. D.; Li, J. L.; Kang, F. Y. Influence of Over-Discharge on the Lifetime and Performance of $LiFePO_4$/Graphite Batteries. *RSC Adv.* **2016**, *6*, 30474−30483.
(37) Castro, L.; Dedryvère, R.; El Khalifi, M.; Lippens, P. E.; Bréger, J.; Tessier, C.; Gonbeau, D. The Spin-Polarized Electronic Structure of $LiFePO_4$and $FePO_4$ Evidenced by in-Lab XPS. *J. Phys. Chem. C* **2010**, *114*, 17995−18000.
(38) Tang, D.; Ji, G. J.; Wang, J. X.; Liang, Z.; Chen, W.; Ji, H. C.; Ma, J.; Liu, S.; Zhuang, Z. F.; Zhou, G. M. A Multifunctional Amino Acid Enables the Direct Recycling of Spent $LiFePO_4$ Cathode Material. *Adv. Mater.* **2023**, *36*, No. 2309722.
(39) Juarez-Robles, D.; Vyas, A. A.; Fear, C.; Jeevarajan, J. A.; Mukherjee, P. P. Overdischarge and Aging Analytics of Li-Ion Cells. *J. Electrochem. Soc.* **2020**, *167*, No. 090558.
(40) Andersson, A. M.; Abraham, D. P.; Haasch, R.; MacLaren, S.; Liu, J.; Amine, K. Surface Characterization of Electrodes from High Power Lithium-Ion Batteries. *J. Electrochem. Soc.* **2002**, *149*, A1358−A1369.
(41) Lu, Y.; Zhao, C. Z.; Huang, J. Q.; Zhang, Q. The Timescale Identification Decoupling Complicated Kinetic Processes in Lithium Batteries. *Joule* **2022**, *6*, 1172−1198.
(42) Steinhauer, M.; Risse, S.; Wagner, N.; Friedrich, K. A. Investigation of the Solid Electrolyte Interphase Formation at Graphite Anodes in Lithium-Ion Batteries with Electrochemical Impedance Spectroscopy. *Electrochim. Acta* **2017**, *228*, 652−658.
(43) Schmidt, J. P.; Chrobak, T.; Ender, M.; Illig, J.; Klotz, D.; Ivers-Tiffée, E. Studies on $LiFePO_4$ as Cathode Material Using Impedance Spectroscopy. *J. Power Sources* **2011**, *196*, 5342−5348.

https://doi.org/10.1021/acsnano.4c03221
ACS Nano 2024, 18, 21125−21134